

UKAEA-CCFE-PR(24)235

Adel Tayeb, Lloyd Fletcher, Mike Gorley, Allan
Harte, Cory Hamelin

Image-based deformation measurements for validation of fusion divertor armour under high heat flux loading

Enquiries about copyright and reproduction should in the first instance be addressed to the UKAEA Publications Officer, Culham Science Centre, Building K1/0/83 Abingdon, Oxfordshire, OX14 3DB, UK. The United Kingdom Atomic Energy Authority is the copyright holder.

The contents of this document and all other UKAEA Preprints, Reports and Conference Papers are available to view online free at scientific-publications.ukaea.uk/

Image-based deformation measurements for validation of fusion divertor armour under high heat flux loading

Adel Tayeb, Lloyd Fletcher, Mike Gorley, Allan Harte, Cory
Hamelin

Image-based deformation measurements for validation of fusion divertor armour under high heat flux loading

Adel Tayeb¹ | Lloyd Fletcher¹ | Mike Gorley² | Allan Harte² | Cory Hamelin²

¹UK Atomic Energy Authority, Fusion Technology Facility, 2A Lancaster Way, Advanced Manufacturing Park, Rotherham, S60 5FX, United Kingdom

²UK Atomic Energy Authority, Culham Science Centre, Abingdon, OX14 3DB, United Kingdom

Correspondence

Dr. Adel Tayeb, UK Atomic Energy Authority, Fusion Technology Facility, 2A Lancaster Way, Advanced Manufacturing Park, Rotherham, S60 5FX, United Kingdom
Email: adel.tayeb@ukaea.uk

Funding information

Engineering and Physical Sciences Research Council (EPSRC), Energy Programme, Grant Number: EP/W006839/1

Engineering components within a fusion reactor are subjected to extreme environments including high heat flux, strong magnetic fields, and neutron irradiation. Simulations are required to predict the in-service lifetimes of fusion components and ensuring credibility of these simulations requires validation over testable domains. Divertors are responsible for extracting heat and ash from the fusion reaction and protecting the vacuum vessel from thermal loads. In this work, we conduct an image-based experimental assessment of a divertor armour component design under a steady-state, high heat flux of $\sim 5 \text{ MW/m}^2$ under vacuum conditions. The heat flux was applied to the water-cooled component using the Heating by Induction to Verify Extremes (HIVE) facility at the UK Atomic Energy Authority. We used digital image correlation (DIC) to measure the surface strain of the component and thermocouples to measure the temperature during the high heat flux pulse. We used synthetic image deformation simulations to analyse sources of random and systematic errors in our DIC measurements and to select DIC processing parameters for subsequent analysis. Our results show that DIC is a valuable tool for the validation of multi-physics simulations by pro-

viding information about the geometrical arrangement of components as well as high resolution data indicating areas of disagreement between the simulation and experiment. The results of our study are the first image-based simulation validation dataset for a divertor component under fusion relevant conditions.

KEY WORDS

Thermo-Mechanical Analysis, Digital Image Correlation (DIC), Simulation Validation, Uncertainty Quantification (UQ), Fusion Engineering

1 | INTRODUCTION

Fusion power is a promising clean energy source that has the potential to replace fossil fuels. Most fusion power plant designs are based on tokamak technology where the plasma is confined by strong magnetic fields in the shape of a torus under vacuum. The components inside of the vacuum vessel of a tokamak that are exposed to the plasma are called plasma-facing components. Their main purpose is to remove heat from the fusion reaction while shielding the vacuum vessel and magnets from high temperatures and neutron irradiation. These components are subjected to cyclic thermal loads on the order of 10's MW/m^2 ; strong electromagnetic fields on the order of several T imparting MN body forces; and neutron irradiation dosages of 10's of dpa [1]. This combination of extreme environmental loads presents a unique challenge in assessing the structural integrity of these components and qualifying them for service.

The qualification of plasma facing components is reliant on simulations as no experimental facility offers component scale testing in a fully representative environment with fusion spectrum neutron irradiation. This implies the need to validate component simulations for credible predictive capabilities [2, 3, 4]. To this end, it is crucial to validate plasma facing component simulations in testable environments and only rely on extrapolating model predictive capabilities in the irradiation domain. Full-scale validation experiments are costly given that the combination of thermal and electromagnetic loading relevant to fusion is difficult to achieve. There are a range of facilities around the world that offer high heat flux testing for plasma facing component at different length scales [5]. UKAEA's Heating by Induction to Verify Extremes (HIVE) facility offers the possibility to test small plasma facing component mock-ups under vacuum conditions and with active water cooling [6]. The Combined Heating and Magnetic Research Apparatus (CHIMERA), which is being built in the UK, will offer testing capabilities for large component mock-ups (up to 1.6 m) under combined high heat flux and strong magnetic fields [7]. The total cost to perform experiments in these facilities is expensive and time consuming. It is therefore crucial to extract the maximum amount of information from experiments to use in model validation. Extracting more data per experiment can be achieved by using image-based measurement techniques such as Digital Image Correlation (DIC). DIC for shape and deformation measurement is well established within the experimental mechanics community for both 2D and stereo DIC measurements [8, 9, 10]. DIC can provide on the order 100,000 spatial data points per set of cameras, which allows for a more robust spatial comparison to finite element (FE) simulations for validation purposes. Furthermore, this technique is readily adapted to a wide range of temperatures from cryogenic [11] to high temperature [12], both of which are relevant to a range of fusion components. For an overview of the use of DIC at high temperature, the reader is referred to the review

by [13].

In recent years, the use of DIC has been extended from the characterization of material and component behaviour to simulation validation. This is due to the full-field nature of the data, which enables quantitative comparison between experiment and simulation in a whole region of interest and not only at discrete locations. Furthermore, uncertainty quantification for DIC systems is becoming established for both 2D and stereo DIC using synthetic image deformation procedures and Monte-Carlo sampling [14, 15, 16]. To date, three main approaches for finite element (FE) simulation validation from full-field measurements have been developed [17, 18, 19, 20]. The first approach relies on a direct field subtraction between the DIC and FE simulation data after interpolating one of the datasets to the same coordinate system [21, 22, 23]. The main drawback of this approach is that it does not account for the bias arising from the low pass filtering effect of the whole DIC measurement chain. The second approach involves using the FE displacement data to synthetically deform images and process them in exactly the same way as the experimental images before performing a field subtraction [14, 15, 19]. Termed FE-levelling in [19], the advantage of this approach is that it adds the DIC bias to the FE data such that it is removed from the comparison when the field subtraction is performed. This method was first introduced for 2D DIC in [14] and then extended to stereo-DIC in [24, 25, 26]. It was then applied to a simulated experiment of a metallic disc under pressure loads in [19] and in the context of Material Testing 2.0 in [27, 28, 20]. The third method of model validation with DIC data is based on image decomposition of the DIC and FE dataset by a set of orthogonal polynomials and then performing the comparison between the identified coefficients from each set of data [17], [18] and [29]. Two types of orthogonal polynomials were mainly used in the literature, namely Zernike in [17] and Chebyshev in [30]. The advantage of this technique is the substantial reduction of the amount of data in the validation process from thousands of data points to a set of coefficients (typically under 20 coefficients). However, a drawback of the method is that it does not account for the bias coming from DIC measurement chain. Given the benefits of using image-based methods to reduce the number of validation experiments these methods have the potential to provide the data required for fusion component qualification over testable multi-physics conditions.

In this work, we collect an image-based dataset for use in simulation validation of a fusion component that is subjected to extreme thermal loads. To this end, we conducted stereo DIC measurements of divertor armour component subjected to high heat flux and coolant flow under vacuum conditions. The component we tested is composed of four tungsten armour blocks brazed to a copper chromium zirconium pipe with a pure copper inter-layer. The component was subjected to a nominal heat flux load on its top surface ranging of 5 MW/m^2 . The heat flux was generated by induction, which resulted in temperatures on the order of 700°C on the top region of the test sample. Strains due to thermal expansion effects were measured by a stereo DIC system adapted to the high temperature environment. We then carried out a thorough uncertainty quantification study using synthetic image deformation simulations to identify the optimal DIC processing parameters to be used as well as investigating sources of random and systematic errors. We then applied the identified processing parameters to the experimental data to extract the strain fields at high temperature to be used in simulation validation. As a first approximation we compare our DIC measurements to an analytical calculation based on the thermocouple measurements and free expansion of the tungsten block. Finally, we conduct a simulation validation analysis comparing our simplified finite element model to our experimental measurements taking into account sources of uncertainty in the experimental measurements. The results of our study present the first high-fidelity image-based simulation validation dataset for a divertor component under fusion relevant conditions.

The paper is structured as follows: Section 2 gives details about the experiment carried out in this study. This includes sample preparation, description of the experiment and DIC setup as well as the experimental procedure. Section 3 describes the data processing steps including the systematic process to select DIC parameters, the noise

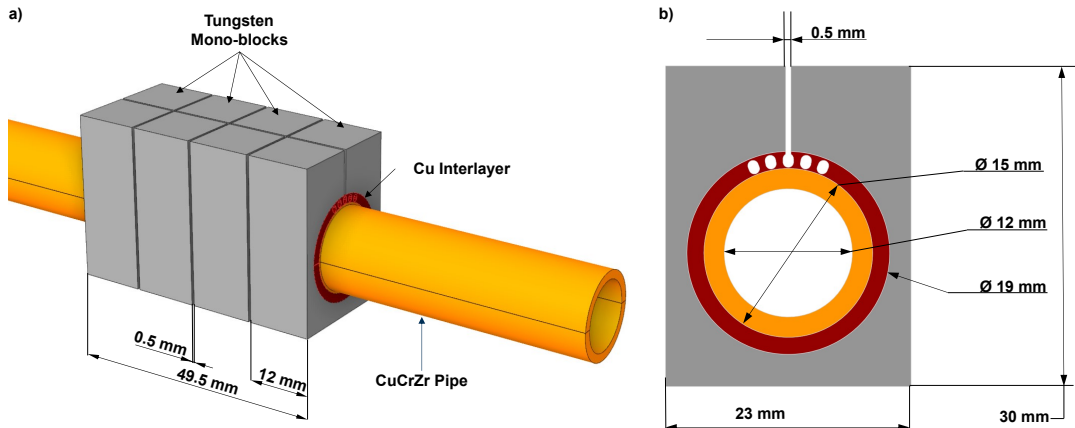


FIGURE 1 Divertor armour component geometry and materials. Perspective view showing axial geometry and materials in a) and a side view in b) showing the armour block, interlayer and pipe geometry.

floor analysis and the bias analysis. Section 4 presents the results and the discussion, this includes the full-field strain maps and thermocouple temperature measurements and the FE model validation. The paper concludes with a summary of the main findings and areas of future work.

2 | METHODOLOGY

2.1 | Sample preparation

The sample geometry we used is depicted in Fig. 1, it is the 'thermal-break' divertor design. It was first introduced in [31] and followed by several studies to reach the final design by assessing its behaviour under high heat flux conditions, with the design being finalized in [32] and [33]. The baseline DEMO (Demonstration Fusion Power Plant) divertor design consists of tungsten blocks that are brazed to a copper chromium zirconium pipe with soft pure copper inter-layer between to account for the mismatch in thermal expansion coefficient. The thermal-break design introduces a split in the top of the armour block and a series of holes in the top of the interlayer to relieve the resulting thermally induced stresses from the mismatch in thermal expansion coefficient between the materials. The manufacturing process is described in [33].

Before the test, we spot welded six K-type thermocouples to the back of the sample in an Argon environment. Given the difficulty of welding to tungsten we required several attempts to attach the thermocouples to the sample as shown in Fig 2a. We then applied a uniform black coating then we applied a random white speckle pattern using an airbrush, see Fig. 2b. The speckle pattern was produced using VHT flame-proof paint to be able to function at temperatures up to 1000° C. Thermocouples TC01, TC03 and TC05 were damaged when the sample was mounted in the test rig so temperature data was only collected from the block with thermocouples TC02, TC04 and TC06.

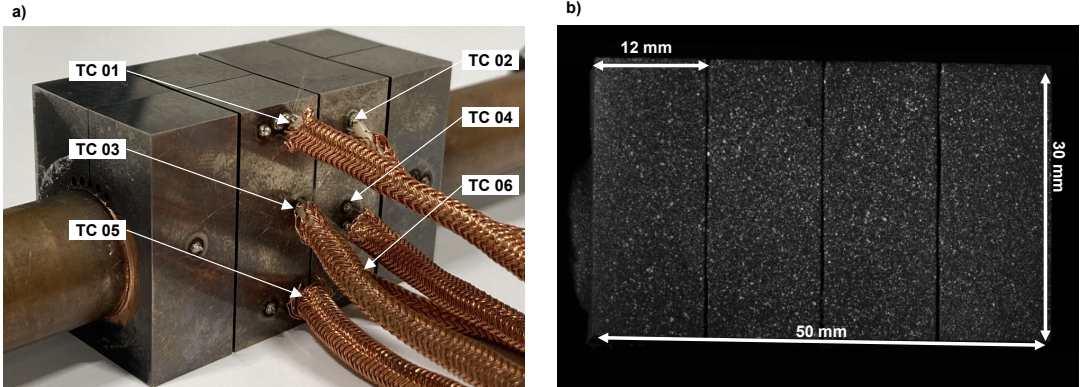


FIGURE 2 Sample preparation showing the thermocouple locations in a) and the speckle pattern applied on the opposing face of the armour block in b)

2.2 | Experimental test rig

The experiment was conducted at UKAEA's *Heating by Induction to Verify Extremes* (HIVE) facility [6]. HIVE is a high heat flux testing facility designed to test small components under fusion relevant surface heat fluxes in vacuum conditions. The HIVE rig is equipped with a high frequency induction heating system that generates a nominal power of 45 kW coupled with a 200 °C, 20 bar closed-loop water cooling system. For a complete overview of the rig, the reader is referred to the technical report [6]. The experimental set-up for our experiment is shown in Fig. 3a, it is composed of the HIVE rig and a stereo DIC system. Both the heating and cooling systems are attached to the HIVE vacuum vessel from the top flange. This flange was used before the test to mount the sample into the cooling loop in the middle of the 500 mm diameter vacuum vessel. The three ø90 mm diameter ports were used for optical diagnostics. This leaves a distance of approximately 300 mm between the sample and the front port. The front port was used for the stereo DIC set-up. The system and its diagnostics are controlled from a separate control room. A close-up of the sample-coil arrangement inside of the vacuum vessel is depicted in 3b. This picture was taken before the test through the left ø90 mm diameter port. We note here that the sample-coil geometrical arrangement strongly affects the efficiency of the induction heating in terms of both magnitude and distribution of the heat flux, as outlined in [34].

2.3 | DIC hardware and setup

We performed all DIC setup and analysis using MatchID v2023.2. A pair of Alvium 1800 U-2460 cameras with a 24 Mpx resolution were used. They were coupled with 50 mm C-mount lenses and blue bandpass filters to mitigate image saturation due to the sample glowing at high temperature. The full DIC setup and hardware parameters are summarized in Table 1. We performed the stereo calibration using a MatchID 9x12 5 mm calibration target. Given the complexity of the test, the calibration was performed once the sample was mounted in place. To this end, a 3D printed holder for this calibration target was designed and used through the left 45° port. We captured 175 pairs of images which we used in the calibration process. The resulting calibration parameters are reported in Appendix A. We note here that the DIC parameters that were used for processing the experimental data are selected in section 3.1 by using synthetic image deformation for uncertainty quantification analysis.

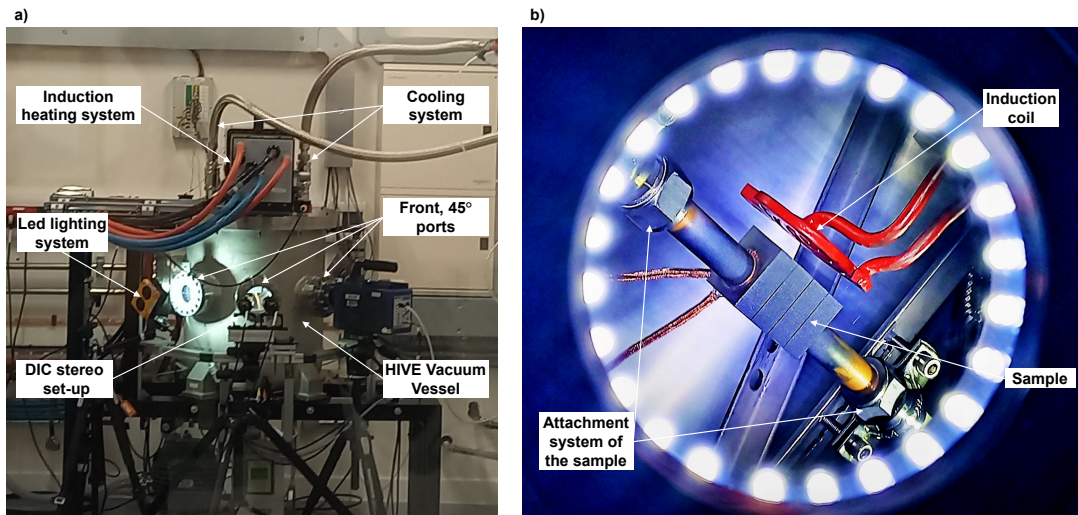


FIGURE 3 Experimental set-up including the Heating by Induction to Verify Extremes (HIVE) facility with DIC hardware in a) and a view through the left hand angles port showing the sample-coil arrangement in b).

TABLE 1 Digital image correlation hardware and associated parameters

Cameras	Alvium 1800 U-2460
Image resolution	5328 × 4608 pixels
Lenses	Edmund Optics 50 mm C-mount
Aperture	f/8
Field of view (FOV)	83.21 × 71.91 mm
Image scale	~ 0.015 mm/pixel
Avg. speckle size	8 pixels, 0.12 mm
Image noise	0.31%
Stand-off distance	335 mm
Filters	Blue bandpass filters
Image acquisition rate	5 Hz
Shutter time	25058 µs

2.4 | Experimental procedure

We applied high heat flux pulses at different nominal power levels to the top surface of the sample and recorded data from the stereo DIC system and thermocouple sensors. While there is no direct measurement of the heat flux applied to the component a nominal heat flux was calculated by assuming the full power provided to the induction system was converted to heat flux. This gives a surface heat flux of approximately 17.2 MW.m^{-2} for the pulse at a nominal input power of 19 kW. The experimental procedure was carried out as follows: after attaching thermocouples and applying the speckle pattern, the sample was mounted to the closed-loop water cooling pipes inside of the HIVE vacuum vessel. Then, the stereo calibration was performed. Once the stereo DIC system was calibrated with an acceptable calibration error, which should be lower than 0.1 according to [24]. The vacuum vessel was then sealed and pumped down to create vacuum conditions (the threshold for the pressure is about 1.10^{-4} millibar). The next step was to acquire a set of static images before and after introducing the coolant flow in order to characterise the noise floor under these conditions. Finally heat flux pulses at increasing power levels were applied while recording all sensor data. The power increase between consecutive pulses was set at 1 kW in order to acquire data before the maximum temperature of the speckle pattern was reached (on the order of 1200° C). The test was stopped after noticeable damage to the speckle pattern which occurred at 24 kW. The coolant conditions were kept constant throughout the test with a temperature of 158° C , a pressure of 0.58 MPa and a flow rate of 5.87 m/s . We recorded each pulse with an image acquisition rate of 5 Hz. This included static images for reference, images during ramp-up, the steady state phase, the ramp-down and set of static images after the pulse. All raw images for the experiment and calibration are attached to the digital dataset.

3 | DATA PROCESSING AND UNCERTAINTY QUANTIFICATION

3.1 | Selection of DIC parameters with image deformation

In this work, we selected DIC processing parameters using a procedure to minimise the difference between the DIC strains and the strain taken from a representative finite element model. The finite element model displacements were processed using a synthetic image deformation simulation to account for the systematic and random errors coming from our DIC measurement chain [14]. We evaluated the image noise from the set of static images recorded before the test using MatchID noise evaluation module. We characterised this noise with a Gaussian distribution with a standard deviation of 2.17 and 2.41 grey levels for camera 0 and camera 1, respectively and a mean of 0 for both cameras. Then, we used the image deformation module of MatchID, based on [14], [15], [35] and [36], to create thirty different copies of deformed noisy images each encoding the simulation results with added homoscedastic noise. We processed these images as if they were experimental data and analysed a range of different combinations of DIC processing parameters to obtain a reasonable trade-off between random and systematic errors.

3.1.1 | Finite element model

We built a simplified finite element (FE) model of the divertor component using ANSYS APDL 2022.R2 to serve as a basis for selecting the DIC processing parameters. The input script for the model can be found in the digital dataset listed at the end of the article. We assumed symmetries in geometry, materials and boundary conditions therefore only one half of a block was modelled, see [37], [38] and [39]. The model consisted of 4280 second order elements. In our model we neglected the small holes in the copper interlayer to reduce meshing complexity and the degrees of

freedom. A bi-linear isotropic hardening model was considered for the three materials. All temperature dependent material properties for the three materials were taken from Appendix A ITER SDC-IC [40], whereas water properties required for calculation of the heat transfer coefficient were taken from [41]. A one way coupling was used to solve the thermo-mechanical simulation starting with the thermal analysis and using the resulting temperature fields as an initial condition for the structural analysis. For the thermal boundary conditions we applied a uniform heat flux to the top surface of 4.67 MW.m^{-2} and then a heat transfer coefficient to the inner surface of the pipe based on Sieder-Tate relationship [42]. We note that the value for the uniform heat flux was based on using an optimiser to minimise the difference between the thermocouple measurements and the temperature at the same location on the finite element model for the pulse at 19 kW . For the mechanical boundary conditions, we applied an internal pressure of 0.58 MPa to the pipe and fixed one of the pipe's ends. We extracted the FE displacement fields U_x and U_y from the side of the tungsten block corresponding to the face where we performed experimental DIC measurements. These displacement fields were then used to deform the experimental reference image of the second block from the left in Fig. 2b.

We note here that the purpose of our FE model was to produce representative strain gradients to aid us in selecting DIC processing parameters whereas a fully fidelity model would explicitly model the induction coil and electromagnetic-thermal coupling to calculate the Joule heating. We will present a full simulation validation in a future work where we can describe this full multi-physics model in detail and perform a validation for varying levels of physics fidelity. In Sec. 4.4 of this paper, we will present a validation attempt to this low fidelity model and highlight differences to the experimental data.

3.1.2 | DIC parameter selection

We analysed different combinations of DIC parameters for each set of noisy images using a grid search method. We fixed several of the DIC processing parameters as reported in Table 2. A parametric sweep of the remaining DIC parameters was performed using the MatchID performance analysis module with the specific combinations of parameters outlined in Table. 3. These combinations led to 96 DIC calculations for each of the 30 copies of noise. We then computed the following cost function for all combinations of parameters as follows:

$$C_E = \sqrt{\sum_{i=1}^N \frac{(E_{xx}^{FE(i)} - E_{xx}^{DIC(i)})^2 + (E_{yy}^{FE(i)} - E_{yy}^{DIC(i)})^2}{2N}}. \quad (1)$$

where E_{xx} and E_{yy} are the in-plane normal strain components, the superscript FE and DIC refer to results from the reference FE solution and the considered DIC combination results, N is the number of data points in the whole region of interest (ROI). Only the xx and yy components of the strain tensor are used as no shearing is expected in this test, i.e. the deformation is due to volumetric thermal expansion. Note that for each DIC combination, the reference FE solution was interpolated to the DIC grid using the griddata function of the scipy interpolate Python. Furthermore, a half strain window at the edge of the ROI was removed from all cost function calculations in order to remove the corrupted edge data that is lost during the DIC procedure. We note that this cost function can be interpreted as the average expected error for the two in-plane strain components.

After analysing the data we found that the cost function was most sensitive to the selection of the subset size and the virtual strain gauge size. Therefore, we fixed the shape function as quadratic, the strain interpolation as Q4 and the step size as 15 pixels. The maps in Fig. 4 correspond to the average cost function \bar{C}_E obtained for each combination of strain window and step sizes (a), its standard deviation $SD(C_E)$ in (b) and the map corresponding to

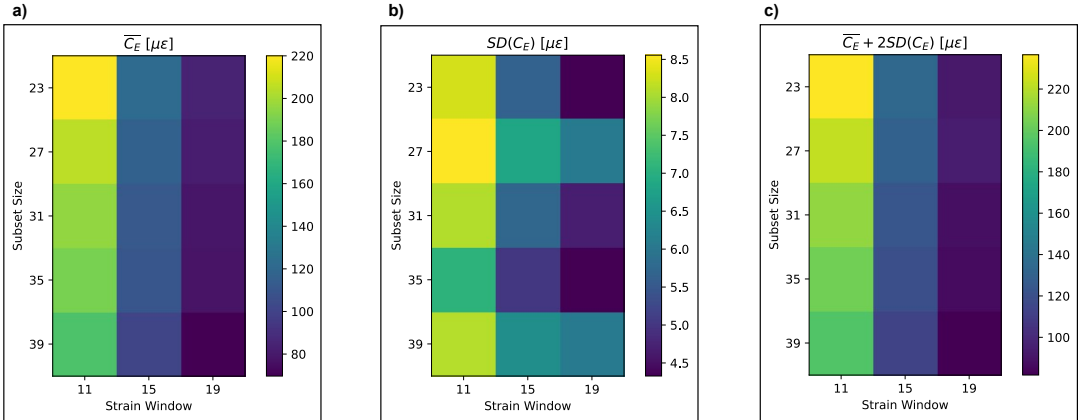


FIGURE 4 Cost function C_E maps as a function of strain window and step sizes, for each combination of strain window and step size the average of C_E was considered: (a) average of the thirty copies of noise, (b) standard deviation and (c) maps corresponding to 95 % confidence interval.

TABLE 2 Common analysis parameters for all DIC analysis

DIC software	MatchId v2023.2
Image filtering	Gaussian 5×5 kernel
Matching criteria	Zero-Normalized Sum of Squared Differences (ZNSSD)
Interpolation	Local Bi-cubic Spline Interpolation
Strain formulation	Logarithmic Euler-Almansi (LEA), $E^{\text{LEA}} = \ln(\sqrt{F \cdot F^T})$
Strains post-filtering	None

the total expected error $|\overline{C_E}| + 2SD(C_E)$ in (c). We used the total expected error to select our DIC parameters in order to obtain a balance between the systematic ($\overline{C_E}$) and random error ($SD(C_E)$). Its lowest value was found in the bottom right corner of the map with a value of $81.76 \mu\epsilon$. For the thirty one considered scenarios (noise-free and thirty copies of noise), the minimum cost function was found for a subset size of 39 pixels , a step size of 15 pixels , a 19 data point strain window corresponding to 4.6 mm and a $Q4$ strain interpolation. We use these DIC parameters for all subsequent analysis in this paper.

3.2 | Noise floor analysis and pattern induced bias

The random error and noise floor analysis in this work was carried out using two different sets of images. The first one was a set of experimental images taken before and after each pulse, i.e. one set of static images per pulse, the second one is a simulated set of 200 synthetic images obtained by adding homoscedastic noise to the reference image of the pulse. For the experimental data sets, we use pulses at a power level equal or less than 19 kW as this was the last pulse before speckle was damaged at the top of the sample due to exceeding the working temperature of the

TABLE 3 DIC sweep parameters considered for the optimization

Parameter	Range	Step	Optimal
Subset size (pixel)	23-39	4	39
Step size (pixel)	10-15	5	15
Shape function	affine-quadratic	-	quadratic
Strain window (data points)	11-19	4	19
strain interpolation	Q4-Q8	-	Q4

paint. The set of experimental images was formed by 197 images taken from images before and after each pulse. This choice was made in order to avoid any rigid body motion caused by the coolant flow, see 4.1 for more details.

Here we focus on the temporal noise floor as it allows us to assess noise induced bias related to the speckle pattern. Furthermore, as the deformation is primarily due to thermal expansion we expect the normal components of strain to be dominant so we will focus on the vertical displacement and strain as they are representative of the other normal components. Information on the other components of the temporal noise floor and the spatial noise floor can be found in Appendix A and the attached digital dataset. The temporal noise floor is calculated as the standard deviation over time of each quantity for each data point in the ROI excluding a half strain window of corrupted edge data. We also calculate the temporal average for each data point to assess any bias.

The temporal average and standard deviation of the vertical displacement U_y is shown in Fig. 5. The average maps are shown in Fig. 5a and 5c for the synthetic and experimental cases with values in the range of -0.41 to 0.41 microns for both. The corresponding temporal noise floors are shown in Fig. 5b and 5d, respectively. The spatial average values of the temporal noise floor of the vertical displacement are $0.40 \mu\text{m}$ and $0.28 \mu\text{m}$ for the synthetic and experimental images. These values corresponds to the typical in plane DIC displacement noise floor of approximately a hundredth of a pixel [16] ($1 \text{ pixel} \sim 22 \mu\text{m}$ for our setup). We note here that we applied rigid body motion correction to the experimental displacement fields to allow comparison between static images before and after each pulse as well as between different pulses. In all these maps, the maximum displacement errors all occur in the same location at top left corner of the block, which is related to a local defect in the speckle pattern.

As the sample is expected to undergo thermal expansion, the shear strains will be small compared to hydrostatic components. Hence, we consider one of the normal components of the strain tensor in this section, namely the vertical component E_{yy} . The temporal average and noise floors for the vertical component of the strain tensor E_{yy} are presented in Fig. 6. The temporal average for this component is shown in Fig. 6a and 6c for synthetic and experimental images, respectively. The temporal noise floor maps are also shown in Fig. 6b and 6d. Here we observe a higher experimental noise floor for the vertical strain component with an average of $31.65 \mu\varepsilon$ compared to $25.57 \mu\varepsilon$ for the synthetic case. The corresponding values for synthetic images are lower for the whole of the ROI. Additionally, the distribution for synthetic images is more random whereas the experimental images are not, which suggests a lower temperature at the end of the pulses with comparison to the starting temperature when the reference image was selected for the correlation.

For the synthetic data in both the vertical displacement and vertical strain components shown in Figs. 5a and 6b we observe that the bias (i.e. the temporal average maps) is low and generally equal to or less than the noise floor. We also analysed convergence of the temporal average and standard deviation for our synthetic data and found no significant difference between a small subset of 50 images and the 200 images we have analysed here. As we have

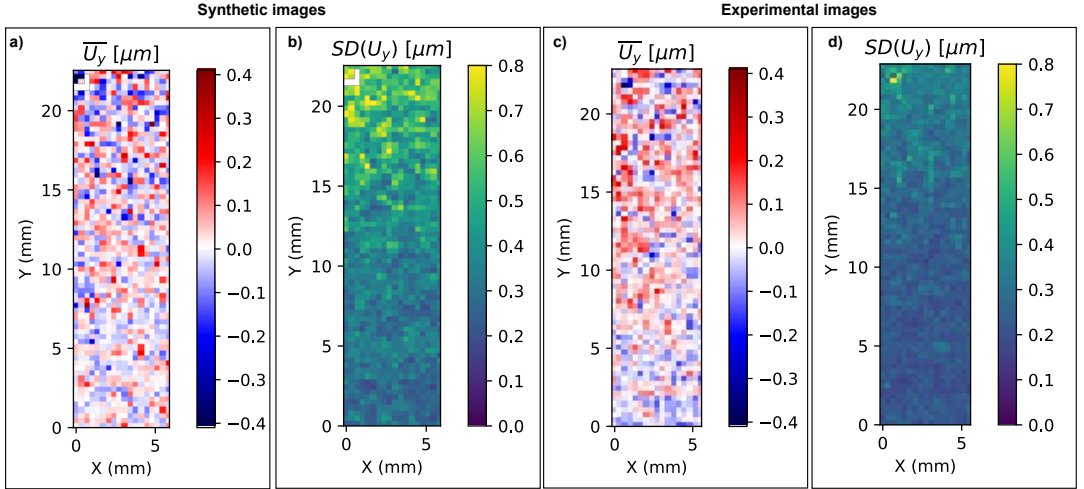


FIGURE 5 Temporal noise floor for the vertical displacement U_y : (a) average and (b) temporal noise floor from synthetic images with an average of $0.4 \mu\text{m}$ and (c) average and (b) temporal noise floor from experimental images with an average of $0.28 \mu\text{m}$.

used an image from the experimental speckle pattern this bias is likely linked to the speckle pattern itself and despite the low magnitude of this error we have corrected all of our subsequent analysis to account for it.

Measurement resolution for DIC is generally taken as a multiple of the noise floor, see [16]. In this work, we chose a multiplier of 4.2 times corresponding to 99.9% of the points in a given population as in [19]. We use the mean of the two resolutions per in-plane normal component for the remainder of this work. Therefore, the displacement resolution is $1.04 \mu\text{m}$ and the strain resolution is therefore $83.16 \mu\varepsilon$. Note that the remaining normal components of the noise floor are reported in Appendix A.

3.3 | Analysis of noise induced bias with image deformation

Here we use synthetic image deformation and our finite element model to compare the strain maps with and without noise in the presence of strain gradients from our finite element model to determine if there is noise induced bias on our measurements. All data presented in this section is produced using image deformation simulations with the speckle pattern from the experiment as the reference image. We carry out this comparison by comparing the vertical strain map for the noise free case to the average strain map extracted from the thirty copies of noise all analysed with the DIC processing parameters selected in the previous section and summarised in Table 2. We ignore corrupted edge data within a half strain window of the edge of the sample and we also correct the strain fields extracted from the noisy cases for pattern induced bias using the average of the temporal noise floor maps shown in the previous section (see Fig. 6c).

In Fig. 7 we show the comparison of the vertical strain fields for the noise free case ' E_{yy}^0 ' in Fig. 7a; average over the thirty copies of noise ' $\overline{E_{yy}^N}$ ' in Fig. 7b; standard deviation over the thirty copies of noise ' $SD(E_{yy}^N)$ ' Fig. 7c, and the error between the average noisy case and the noise free case ' $\overline{E_{yy}^N} - E_{yy}^0$ ' Fig. 7d. For the vertical strain maps in Fig. 7a and Fig. 7b we observe that the noise-free and average of the noisy case are qualitatively similar. Additionally, if we compare the noise floor predicted by analysis of static synthetic images in Fig. 6b and the standard deviation over the

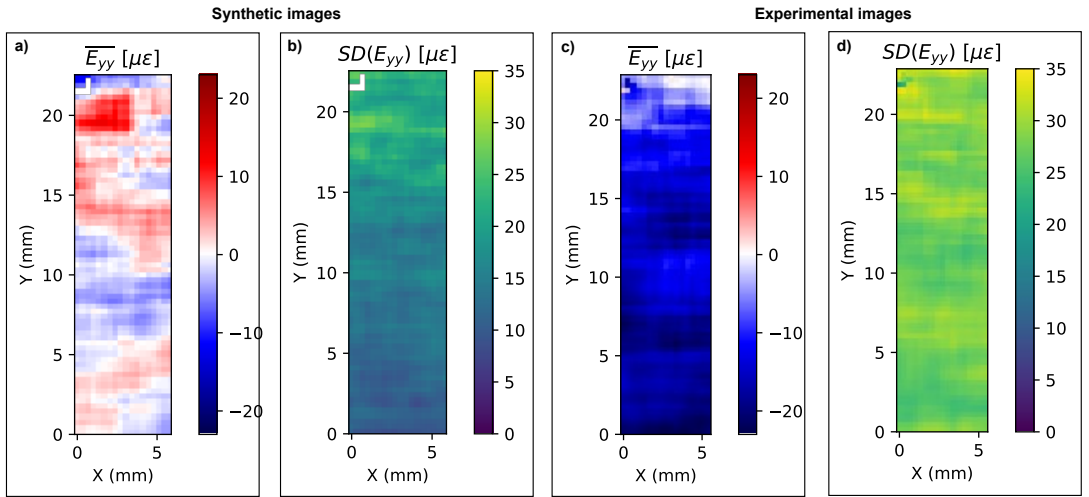


FIGURE 6 Temporal noise floor for the vertical strain field E_{yy} : (a) average and (b) temporal noise floor from synthetic images with an average value of $25.57 \mu\epsilon$ and (c) average and (d) temporal noise floor from experimental images with an average value of $31.65 \mu\epsilon$.

thirty copies of noise we observe that the noise floor for static images is approximately half the standard deviation observed . This difference is most likely a result of the smaller number of images analysed for the analysis which is 30 images in Fig. 7 versus 200 images in Fig. 6. Finally, in Fig. 7d we observe that for the noisy case the strains at the top of the block are systematically over estimated by up to $\sim 70 \mu\epsilon$. However, this difference is on the order of the measurement resolution and the standard deviation over the thirty copies of noise in Fig. 7c so is unlikely to be significant.

In Fig. 8 we show the strain profile along the middle line of the block under steady state conditions. In this figure the bounds for the no noise case are taken as the measurement resolution ($4.2 SD$) extracted from analysis of static images in Sec. 3.2. For the noisy case the bounds are based on the 4.2 times the standard deviation over the thirty copies of noise. If there is no noise induced bias then the average strain profile for the thirty copies of noise should closely agree with the no noise case. This is what we observe at the base of the block where the strain gradient is low and there is minimal difference between the noise free and noisy image deformation cases. Towards the top of the block where the strain gradient is steeper we observe a slight overestimate for the average of the noisy data but this does not exceed our measurement resolution. With this analysis we have shown that there is no significant noise induced bias coming from our experimental speckle pattern when it is synthetically deformed using our simplified finite element model. This means that we can use the noise-free synthetic image deformation data as a reference to validate our simulation against our experimental data in a similar manner to Lava et al. [19].

4 | EXPERIMENTAL RESULTS

4.1 | Test geometry and sample rigid body motion

The effectiveness of induction heating is strongly dependent on the geometry of the induction coil, the geometry of the sample being heated and their relative positions and orientations with respect to each other [34]. Here we

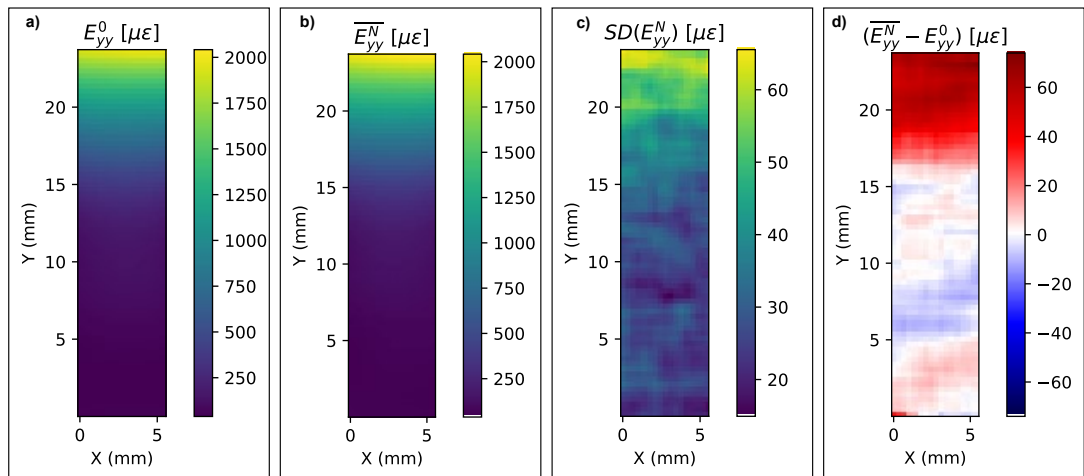


FIGURE 7 Maps of the vertical component of the strain from noise-free data ' E_{yy}^0 ' in a); average from thirty copies of noise ' $\overline{E_{yy}^N}$ ' in b); standard deviation over the thirty copies of noise ' $SD(E_{yy}^N)$ ' in c); and the difference between the noise-free and average over all noisy cases ' $\overline{E_{yy}^N} - E_{yy}^0$ ' in d).

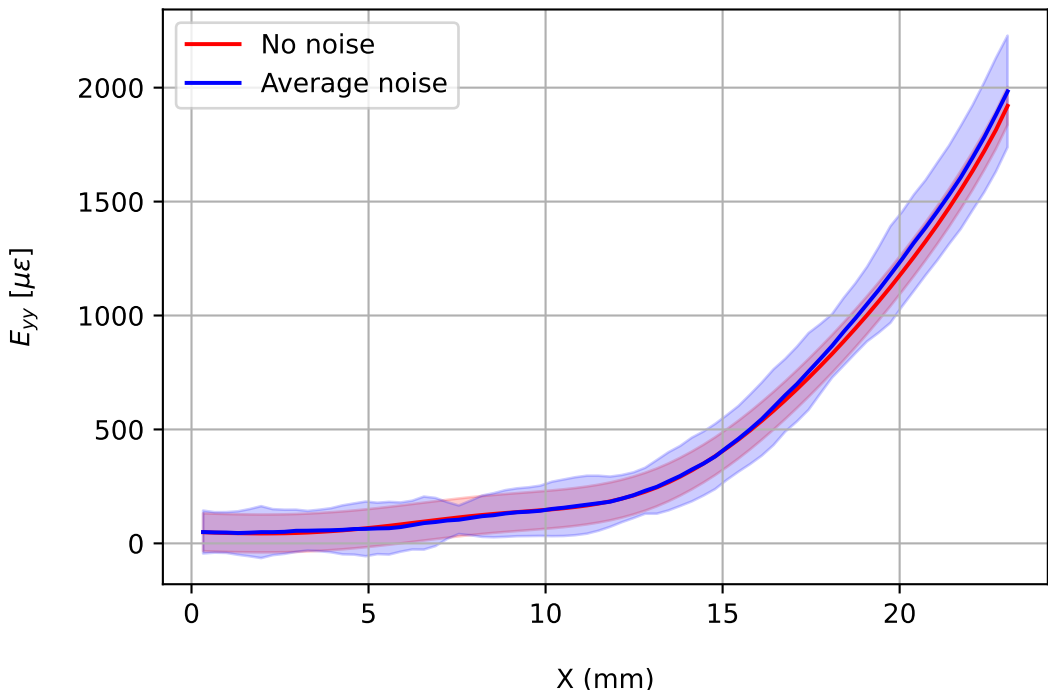


FIGURE 8 Profile plots of the vertical strain component for the no noise case ' E_{yy}^0 ', where the shaded bounds are the measurement resolution of 4.2 SD and the noisy case ' E_{yy}^N ', where the shaded bounds indicate 4.2 SD over the thirty copies of noise analysed.

use DIC data from our tests to analyse and extract the relative positions and orientations of the sample with respect to the coil throughout the test to aid in future simulation validation efforts. Fig. 9 shows the measured geometrical arrangement between the induction coil and the test sample before and throughout the pulse. It can be seen from Fig. 9a that the sample is not perpendicular to the coil plane. The deviation of the sample from the perpendicular plane to the coil plane was 9.26° before the pulse. In Fig. 9b we show the distance from the centroid of the induction coil measurement area to the centroid of the measurement area of the block in the X, Y and Z directions. In Fig. 9c we show the distance change in all components between the centroids of the measurement areas of the block and coil. To obtain these distances, each component of the coordinates of the coil and block were averaged in space over their corresponding areas at each time step. The relative distance change reached $300\mu\text{m}$ in the X direction, $205\mu\text{m}$ in the Y direction and $150\mu\text{m}$ in the Z direction. The behaviour was different for each component. In the X direction, no clear maximum was reached before the end of the pulse with small high frequency fluctuations throughout the pulse. The distance in the Y direction was more stable and reached its maximum relatively fast after the start of the pulse with no apparent fluctuations. Finally, the distance change in the Z direction exhibited large fluctuations (between 100 and $150\mu\text{m}$) with a higher frequency compared to the X direction. We note that these rigid body movements are an order of magnitude higher than displacement noise floors reported in Table 5. Given the turbulent cooling water flow through the internal pipe it is likely the oscillations in these traces are due to fluid-induced vibration. The main component of the rigid body motion during the test is most likely due to electro-mechanical coupling given that the Y and Z position returns after the end of the pulse.

In this section we have demonstrated a key motivation for using image-based measurements for component validation experiments. In our case we would have been blind to the exact orientation and position of the test sample with respect to the coil without access to image-based measurements. In the future we will use the result shown in Fig. 9 to impose the experimental geometrical arrangement on our simulation for a thermal-electromagnetic FE model to obtain the true heat flux and temperature distribution in the entirety of the sample throughout the pulse. We will also analyse the sensitivity of the model with respect to the rigid body motion during the pulse (as shown in Fig. 9c) to determine if modelling this behaviour is required for validation.

4.2 | Thermocouple temperature measurements

In this section we present the temperature measurements carried out during the pulse at 19 kW using the thermocouples attached to the back of the sample. We note that only thermocouples TC 02, TC 04 and TC 06 recorded measurements during the heat flux pulses (see Fig. 2) due to sensor failures during the sample mounting process. We show the thermocouple temperature traces for the full duration of the 19 kW pulse in Fig. 10. Before each pulse we observe that the temperature recorded from all thermocouples matched the coolant flow temperature at approximately 150°C indicating the component was initially at a uniform temperature. From all thermocouples we observe an exponential rise in temperature over approximately 5 s to the steady state value. The maximum temperature recorded from TC 02 was 510°C , 249°C from TC 04 and 168°C from TC 06 with the highest temperature observed near the top of the armour block and lower temperatures close to the bottom of the block where the cooling pipe was located as expected based on our test setup.

Directly after the pulse the temperature exponentially decayed back towards the coolant temperatures over approximately 8 s. We note that the exponential temperature rise and fall is an expected response for induction heating [34]. By closely observing the thermocouple traces we noticed that there was a subtle linear increase in temperature throughout the steady state portion of the pulse followed by an offset once the induction heating was stopped. This offset was more prominent for the thermocouples closer to the top of the block and disappeared between pulse with

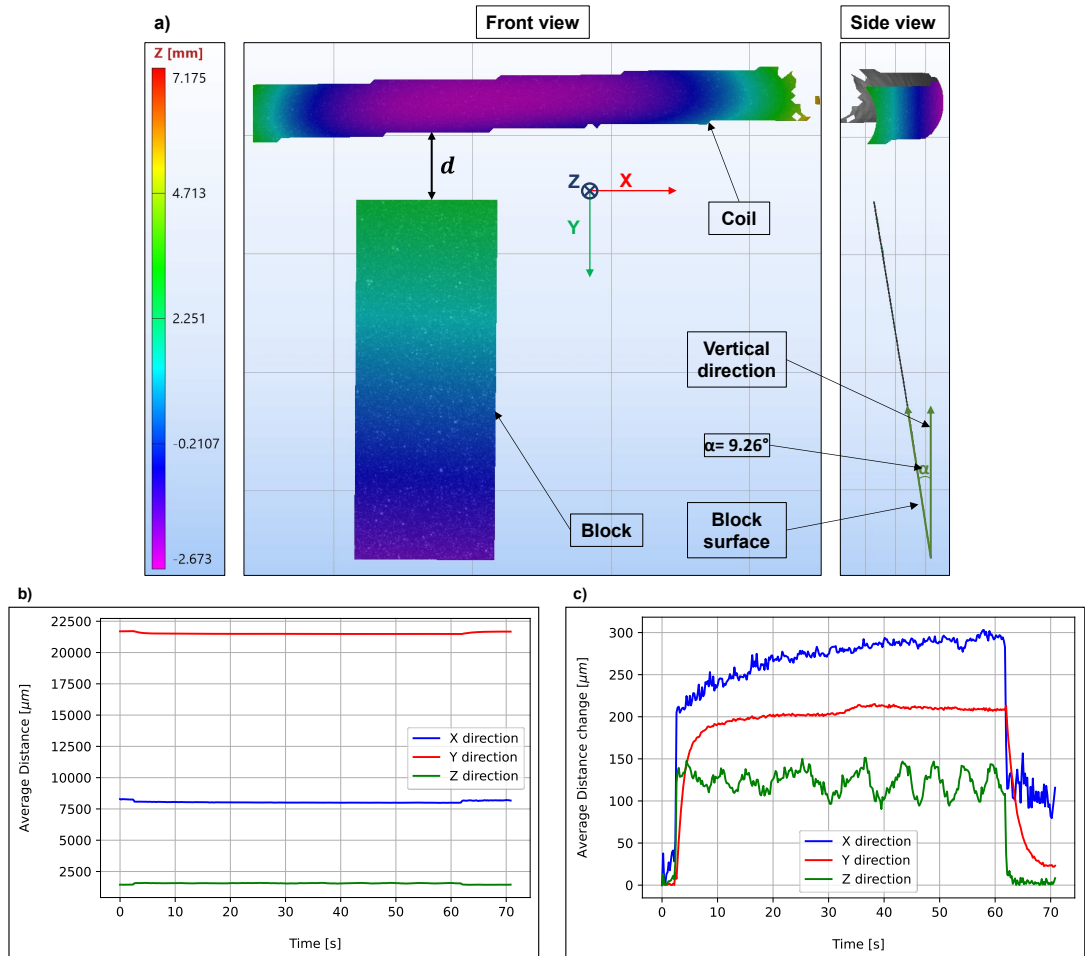


FIGURE 9 Geometric coil-sample arrangement before the pulse (a) and distance between the block and the coil centroids throughout the pulse (b) and centroids distance change during the pulse (c).

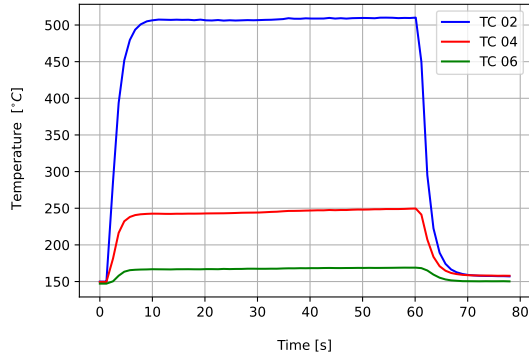


FIGURE 10 Experimental temperature recorded during the pulse at 19 kW from all active thermocouples.

the thermocouples all returning to the coolant temperature within approximately 3 minutes.

If we assume the strain in the sample is only due to thermal expansion then we can convert the temperatures measured with the thermocouples to an equivalent thermal strain through (ε^{th}) the thermal expansion coefficient, as follows:

$$\varepsilon^{th} = \alpha^{se}(T)(T - T_{ref}), \quad (2)$$

where, $\alpha^{se}(T)$ is the secant coefficient of thermal expansion at temperature T and T_{ref} is its reference temperature. Additionally, we make the assumption that the sample is purely composed of tungsten and use the temperature dependent thermal expansion coefficient taken from Appendix A of the ITER SDC-IC [40] for tungsten. We note that these assumptions will be most accurate at the top of the tungsten block where the sample can freely expand and is further from the multi-material interface at the pipe. Closer to the pipe this assumption will be less representative but is suitable for a first order comparison to our DIC measurements in the following section assuming symmetry between the front and back faces of the component.

4.3 | Comparison of DIC strain to the thermocouple measurements

Here we compare the strain we have measured using DIC to the strain calculated from the thermocouple traces using the assumptions discussed in the previous section. In Fig. 11 we show this comparison. To perform a comparison between data obtained from the back of the block using the thermocouples and data obtained from the front of the block with DIC we need to make two assumptions: 1) that the thermal and kinematic fields are symmetric about the centre line of the pipe; and 2) the strains on the front face of the block are due solely to thermal expansion. The thermocouple traces were recorded on the data acquisition system used for machine control whereas the DIC cameras were controlled by a dedicated image capture computer with a different clock. Therefore, we temporally aligned the traces by identifying the first point at which there was a sharp continuous rise in the signal above the measurement resolution and aligning this point between the DIC and thermocouple traces. As the thermocouple traces have the lowest sampling frequency of approximately 1 Hz the temporal alignment error is on the order of 0.5 s. We analysed the thermocouple traces with Eq. 2 and extracted average thermal strains over the steady state response of 1705 $\mu\epsilon$.

for TC 02, $456 \mu\epsilon$ for TC 04 and $82 \mu\epsilon$ for TC 06.

In Figs. 11 a) to c) we show comparison traces from the average of the two normal components of the strains measured with DIC ' $E_{xx} + E_{yy}/2$ ' to the strain calculated using the thermocouple temperatures and Eq. 2. Note that for these traces the uncertainty bound for the DIC data is the measurement resolution given in Tab. 5. We show the vertical strain field from the experimental data averaged over the steady state portion of the pulse (285 images between times $t = 5$ s and $t = 62$ s) in Fig. 11d with the red dots showing the equivalent location of the thermocouples on the same face as the DIC data. Finally, in Fig. 11 we show the temperature field calculated from the DIC strains using Eq. 2. In comparing the traces in Figs. 11 a) to c) we see that the DIC data and the thermocouple traces are in agreement for TC02 at the top of the block. As we move down the block the signal to noise ratio for the DIC data becomes worse and there is a deviation between the DIC data and thermocouples which is most pronounced for TC04. As TC04 is located near the top of the interface between the pipe and the armour block we expect it to exhibit the most deviation from our assumptions. This results from the top surface of the pipe having the highest temperature on pipe surface (as it is closest to where the heat flux is applied) leading to the highest mismatch in thermal expansion between the three constituent materials. At the top of the block where TC02 is located our assumptions are more likely to be valid as this location behaves more like a tungsten block freely expanding. However, the agreement between the DIC data and TC02 is also surprising as we know that the real test geometry should lead to asymmetry in the induction heating profile at the top of the block (see Sec. 4.1 and Fig. 9). We will investigate the sensitivity to asymmetry in the temperature field as future work using a full electromagnetic-thermal simulation including an explicit model of the induction coil. We also note here that the asymmetry due to the geometric arrangement may be localised to the top corner of the armour block and fall off rapidly. In this case TC02 might be too far from the top surface to be able to detect the asymmetry. Finally, the temperature field calculated from the DIC strains shown in Fig 11 shows a peak equivalent temperature of approximately $700^\circ C$. In this section we have successfully cross validated our experimental measurements by comparing the strains measured with DIC to the strains calculated using the thermocouple traces. In the next section we will attempt to use our DIC data and image deformation simulations to validate our simplified FE model.

4.4 | Simulation Validation Analysis

In this section we attempt to validate our simplified finite element model against the strain fields we have measured using DIC. We note here that as we have used the thermocouple measurements to calibrate the value of the uniform heat flux applied in our simulation we cannot use the thermocouple data for validation purposes. To account for systematic errors in the DIC measurement chain we use the synthetic image deformation simulation for the case without noise as our reference to compare to our experimental data following a similar procedure to Lava et al. [19]. Our validation analysis is summarised in Fig. 12 for the vertical strain component. In Fig. 12a we show the experimental strain fields ' E_{yy}^{EXP} ' averaged over 285 steady state images (taken between times $t = 5$ s and $t = 62$ s) during the $19 kW$ pulse and in Fig. 12b we show the corresponding strain fields for the noise free synthetic image deformation simulation ' E_{yy}^{SIM} '. The difference between the experimental and the synthetic image deformation is shown in Fig. 12c and dividing the difference map by the standard deviation and thresholding by the measurements resolution of 4.2 times the standard deviation is shown in Fig. 12d.

In an initial comparison of Figs. 12a and b we see that the model qualitatively matches the shape of the underlying strain fields. However, when we subtract the strain fields between the experimental data and synthetic image deformation we clearly observe a significant difference at the top of the block where the induction heating is applied. This difference is above $100 \mu\epsilon$ in the top quarter of the block and exceeds the measurement resolution in this region

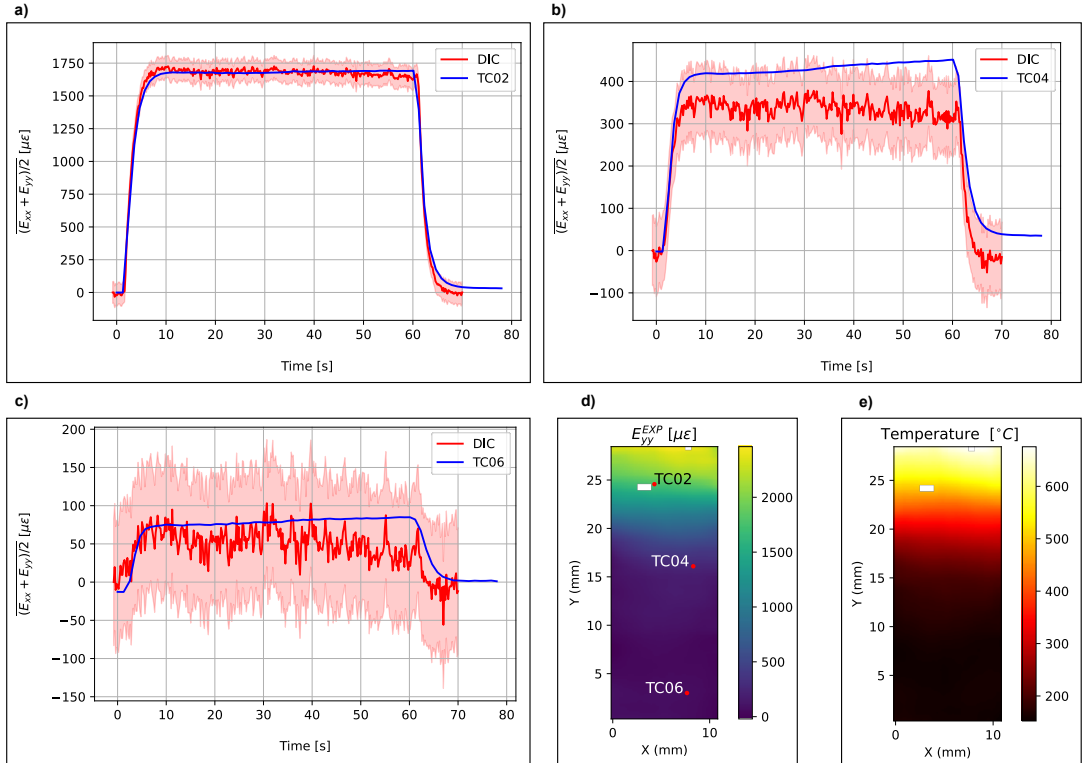


FIGURE 11 Comparison between strain measured with DIC to the strains calculated using the thermocouples and Eq. 2: TC02 in a), TC04 in b), and TC06 in c). The vertical strain map along with thermocouples locations is shown in d) and temperature distribution calculated from the DIC strains based on Eq. 2 in e). Note that for the traces in a) to c) the shaded area for the DIC data is the measurement resolution.

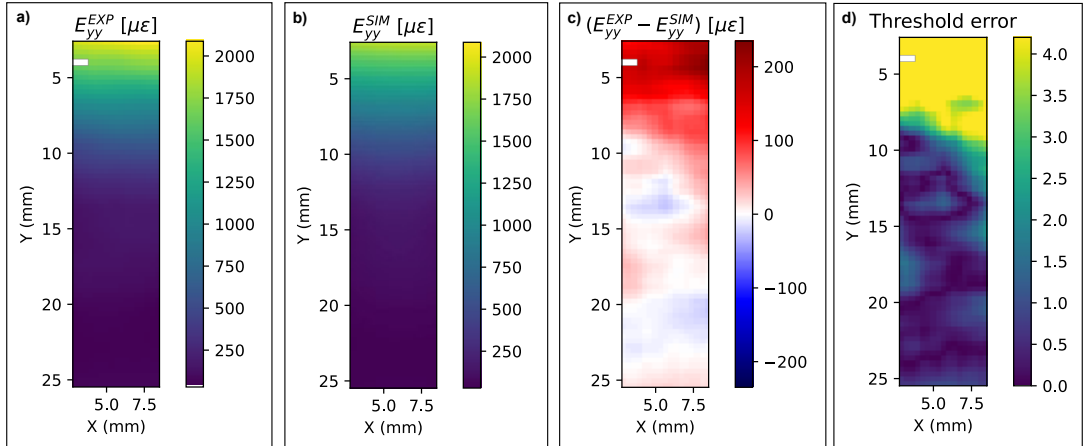


FIGURE 12 Model validation analysis showing the vertical strain map from the experiment E_{yy} averaged during steady state ($t = 5$ s to $t = 62$ s) in a), the vertical strain maps from synthetic image deformation without noise E_{yy}^{SIM} in b), the difference between the experimental and synthetic image deformation strain maps in c), and the difference map in c) divided by the standard deviation with a threshold of the measurement resolution of 4.2 SD in d).

as shown in Fig 12d. Overall, this analysis suggests our current simplified model is not valid for predicting the thermal strain at the top of the armour block which is likely a result of the assumptions we made in our finite element simulation compared to the experiment.

In constructing our finite element model we assumed symmetry on the face of the block where we performed our DIC measurements and the opposing face where the thermocouples are located (see Fig. 2). Given the geometrical analysis from our DIC data in Sec. 4.1 which shows the block is at an angle of 9.26° to the vertical we would expect the heat flux distribution on the top surface to be asymmetric as the top surface of the block will not be parallel to the induction coil. Furthermore, we assumed the heat flux distribution on the top surface of the block was uniform whereas the interaction between the induction coil and the sample will produce a non-uniform heat flux [34]. This non-uniform heat flux will occur even if the top surface of the armour block is parallel to the induction coil as we would expect the heat flux distribution to exhibit sharp concentrations where the induction coil overlaps the corners of the tungsten armour blocks. Despite the difference at the top of the block we note that the strains further down the block near the coolant pipe axis match between the experiment and model. This suggests that the heat transfer coefficient for the coolant in the pipe specified in the simulation is likely to be reasonable or this could also indicate we do not have enough resolution to detect differences in this region due to the small strain levels. It is also possible that the temperature dependent thermal expansion coefficient we used in our model does not accurately represent the experimental material. However, given the match near the base of the block this deviation would have to occur only at higher temperatures near the top of the block so is unlikely.

In summary, we have shown our simplified symmetric finite element model with a uniform heat flux does not accurately predict the strains at the top of the armour block. In the future we will use a full electromagnetic-thermal-mechanical simulation which explicitly models the induction coil including the relative position of the sample with respect to the coil to determine if we can validate with increased model fidelity.

5 | CONCLUSION

In this work, we carried out image-based deformation measurements of a fusion heat-sink component subjected to high heat flux loading with the aim to obtain high quality data to be used for model validation. The kinematic fields were measured by a stereo-DIC system adapted to high temperatures and vacuum environments and the temperature of the component was measured by K-type thermocouples attached to the back of the sample. We then performed a thorough uncertainty quantification to assess systematic and random errors coming from the DIC measurement chain and to identify the optimal DIC parameters to use in these conditions. Our key findings can be summarised as follows:

- We analysed static images from our experiments and created synthetic noisy static images to analyse random errors and pattern induced bias from our DIC measurement system and used this to for subsequent quantitative analysis.
- We used image deformation simulations to select DIC parameters that gave us the minimum error with respect to the ground truth taken from our simplified finite element model.
- Our image deformation simulations showed that the strain fields do not include any significant noise induced bias such that the image deformation strain fields from the noise-free case can serve as a reference for model validation analysis.
- We showed that the experimental image-based measurements provided essential information about the geometrical arrangement of components and boundary conditions. We showed that the component orientation was not perpendicular to the induction coil and the average distance between the component and the induction coil changed during the pulse.
- We compared our thermocouple measurements to our measured strains with DIC assuming pure thermal expansion and found reasonable agreement at the top of the block where the signal to noise ratio of the DIC measurements was high and the assumptions of the analysis were more likely to be valid.
- Using a comparison of our experimental strain fields to the synthetic image deformation simulation without noise we showed our simplified model is invalid for predicting strains at the top of the armour block. This is most likely due to the geometric asymmetry of the experiment and non-uniform heat flux from induction heating.

In a follow up study we will use the results presented in this paper and the associated uncertainty quantification analysis to perform a sequential validation of finite element models of increasing fidelity. We will begin this analysis by explicitly modelling the induction coil in an electromagnetic-thermal analysis assuming that the top surface of the sample is placed perpendicular to the induction coil plane. We will then account for the exact orientation of the sample with respect to the induction coil. For all of these cases we will be able to perform a two stage validation by first comparing the electromagnetic-thermal analysis to the thermocouple measurements and then the strain fields from the thermal-mechanical coupling to the DIC measurements. In summary, we have shown that DIC measurements are a valuable data-rich tool that can provide a large database for simulation validation analysis even in the challenging environments required for analysis of fusion components.

Parameter	Value
F_x Camera 0 [pixels]	19447
F_y Camera 0 [pixels]	19449
F_s Camera 0 [pixels]	4
κ_1 Camera 0	-0.1983
κ_2 Camera 0	-1.1775
κ_3 Camera 0	25.011
C_x Camera 0 [pixels]	2622
C_y Camera 0 [pixels]	2292
F_x Camera 1 [pixels]	19488
F_y Camera 1 [pixels]	19487
F_s Camera 1 [pixels]	-3
κ_1 Camera 1	-0.1868
κ_2 Camera 1	-1.1657
κ_3 Camera 1	25.756
C_x Camera 1 [pixels]	2656
C_y Camera 1 [pixels]	2255
T_x [mm]	-76.16
T_y [mm]	0.37
T_z [mm]	6.68
θ [°]	-0.18
ϕ [°]	11.22
ψ [°]	-0.27

TABLE 4 Stereo DIC calibration parameters.

TABLE 5 DIC noise floor and resolution. The noise floor is taken as the standard deviation (SD) and the resolution is taken as 4.2 times the temporal SD.

Quantity	Spatial noise floor (SD)	Temporal noise floor (SD)	Resolution (4.2 SD)
$U_x (\mu\text{m})$	0.22	0.20	0.84
$U_y (\mu\text{m})$	0.28	0.30	1.17
$\overline{U_x + U_y} (\mu\text{m})$	0.25	0.25	1.01
$U_z (\mu\text{m})$	2.84	4.28	18.0
$E_{xx} (\mu\epsilon)$	16.2	24.2	68.0
$E_{yy} (\mu\epsilon)$	23.4	27.8	98.3
$\overline{E_{xx} + E_{yy}} (\mu\epsilon)$	19.8	26.0	83.2

A | DIC CALIBRATION, PROCESSING PARAMETERS AND NOISE FLOORS.

Acknowledgement

The authors thank Engineering and Physical Sciences Research Council (EPSRC) for funding this work (grant number EP/W006839/1). The authors want to acknowledge the HIVE operation team for their support: James Paterson, Stephen Cosser, Ella Bartley, Joshua Whitley and Enrico Marcucci. We would also like to thank Tom Barrett for provision of the samples for this test.

conflict of interest

The authors declare no conflict of interests.

Supporting Information

Supporting information and data are available here: <https://doi.org/10.5281/zenodo.14021466>

references

- [1] You J, Mazzone G, Visca E, Greuner H, Fursdon M, Addab Y, et al. Divertor of the European DEMO: Engineering and technologies for power exhaust. *Fusion Engineering and Design* 2022;175:113010.
- [2] Schwer LE. Guide for verification and validation in computational solid mechanics 2009;.
- [3] Oberkampf WL, Roy CJ. Verification and validation in scientific computing. Cambridge university press; 2010.
- [4] Kaizer J. Credibility Assessment Framework for Critical Boiling Transition Models: A Generic Safety Case to Determine the Credibility of Crucial Heat Flux and Critical Power Models. US Nuclear Regulatory Commission, Office of Nuclear Reactor Regulation; 2019.
- [5] Lindquist EG. High Heat Flux Testing Facilities and an Electrothermal-Arc Plasma Source for Plasma-Material Interaction Studies and Diagnostic Development 2020;.

- [6] Pearl J, Paterson J, Flinders K, Mantel N, You JH. Cyclic medium heat flux testing of a WTa lattice structure on the HIVE facility. *Fusion Engineering and Design* 2023;194:113699.
- [7] Barrett T, Bamford M, Chulion B, Deighan T, Efthymiou P, Fletcher L, et al. The CHIMERA facility development programme. *Fusion Engineering and Design* 2023;194:113689.
- [8] Sutton MA, Orteu JJ, Schreier H. *Image correlation for shape, motion and deformation measurements: basic concepts, theory and applications*. Springer Science & Business Media; 2009.
- [9] Pan B. Recent progress in digital image correlation. *Experimental mechanics* 2011;51:1223–1235.
- [10] Hild F, Roux S. Digital image correlation. *Optical methods for solid mechanics A full-field approach* 2012;367:183–228.
- [11] Yang J, Li Y, Deng J, Zhang Z, Zhou J, Zhang X. Novel Speckle Preparation and Heat Insulation Method for DIC Strain Measurement at Cryogenic Temperature and Large Deformation Environment. *Experimental Mechanics* 2024;64(1):73–84.
- [12] Pan Z, Huang S, Su Y, Qiao M, Zhang Q. Strain field measurements over 3000 C using 3D-Digital image correlation. *Optics and Lasers in Engineering* 2020;127:105942.
- [13] Yu L, Pan B. Overview of high-temperature deformation measurement using digital image correlation. *Experimental Mechanics* 2021;61(7):1121–1142.
- [14] Lava P, Cooreman S, Coppieeters S, De Strycker M, Debruyne D. Assessment of measuring errors in DIC using deformation fields generated by plastic FEA. *Optics and Lasers in Engineering* 2009;47(7-8):747–753.
- [15] Lava P, Cooreman S, Debruyne D. Study of systematic errors in strain fields obtained via DIC using heterogeneous deformation generated by plastic FEA. *Optics and Lasers in Engineering* 2010;48(4):457–468.
- [16] Jones EM, Iadicola MA, et al. A good practices guide for digital image correlation. *International Digital Image Correlation Society* 2018;10:1–110.
- [17] Wang W, Mottershead JE, Sebastian CM, Patterson EA. Shape features and finite element model updating from full-field strain data. *International Journal of Solids and Structures* 2011;48(11-12):1644–1657.
- [18] Sebastian C, Hack E, Patterson E. An approach to the validation of computational solid mechanics models for strain analysis. *The Journal of Strain Analysis for Engineering Design* 2013;48(1):36–47.
- [19] Lava P, Jones EM, Wittevrongel L, Pierron F. Validation of finite-element models using full-field experimental data: Levelling finite-element analysis data through a digital image correlation engine. *Strain* 2020;56(4):e12350.
- [20] Peshave A, Pierron F, Lava P, Moens D, Vandepitte D. Metrics to evaluate constitutive model fitness based on DIC experiments. *Strain*;p. e12473.
- [21] Tayeb A, Le Cam JB, Grediac M, Toussaint E, Robin E, Balandraud X, et al. Identifying hyperelastic constitutive parameters with sensitivity-based virtual fields. *Strain* 2021;57(6):e12397.
- [22] Tayeb A, Di Cesare N, Lu Y, Sales L, Bastos G, Le Cam JB. Identifying simultaneously hyper-viscoelastic parameters from a unique heterogenous relaxation test: application to engineering elastomeric materials. *Meccanica* 2023;58(10):1983–2002.
- [23] Callaghan JS, Crump D, Nielsen AS, Thomsen O, Dulieu-Barton JM. Quantitative full-field data fusion for evaluation of complex structures. *Experimental Mechanics* 2023;63(7):1095–1115.
- [24] Balcaen R, Wittevrongel L, Reu P, Lava P, Debruyne D. Stereo-DIC calibration and speckle image generator based on FE formulations. *Experimental Mechanics* 2017;57:703–718.

- [25] Dufour JE, Beaubier B, Hild F, Roux S. CAD-based displacement measurements with stereo-DIC: principle and first validations. *Experimental Mechanics* 2015;55:1657–1668.
- [26] Dubreuil L, Dufour JE, Quinsat Y, Hild F. Mesh-Based Shape Measurements with Stereocorrelation: Principle and First Results. *Experimental Mechanics* 2016;56:1231–1242.
- [27] Rossi M, Lava P, Pierron F, Debruyne D, Sasso M. Effect of DIC spatial resolution, noise and interpolation error on identification results with the VFM. *Strain* 2015;51(3):206–222.
- [28] Wang P, Pierron F, Rossi M, Lava P, Thomsen O. Optimised experimental characterisation of polymeric foam material using DIC and the virtual fields method. *Strain* 2016;52(1):59–79.
- [29] Dvurecenska K, Diamantakos I, Hack E, Lampeas G, Patterson EA, Siebert T. The validation of a full-field deformation analysis of an aircraft panel: A case study. *The Journal of Strain Analysis for Engineering Design* 2021;56(4):265–272.
- [30] Patterson EA, Diamantakos I, Dvurecenska K, Greene RJ, Hack E, Lampeas G, et al. Validation of a structural model of an aircraft cockpit panel: An industrial case study. *The Journal of Strain Analysis for Engineering Design* 2022;57(8):714–723.
- [31] Barrett T, McIntosh S, Fursdon M, Hancock D, Timmis W, Coleman M, et al. Enhancing the DEMO divertor target by interlayer engineering. *Fusion Engineering and Design* 2015;98:1216–1220.
- [32] You J, Visca E, Bachmann C, Barrett T, Crescenzi F, Fursdon M, et al. European DEMO divertor target: Operational requirements and material-design interface. *Nuclear materials and Energy* 2016;9:171–176.
- [33] Lukenskas A, Barrett T, Fursdon M, Domptail F, Schoofs F, Greuner H, et al. High heat flux test results for a thermal break DEMO divertor target and subsequent design and manufacture development. *Fusion Engineering and Design* 2019;146:1657–1660.
- [34] Tsopelas N, Siakavellas NJ. Influence of some parameters on the effectiveness of induction heating. *IEEE Transactions on magnetics* 2008;44(12):4711–4720.
- [35] Rossi M, Pierron F. On the use of simulated experiments in designing tests for material characterization from full-field measurements. *International Journal of Solids and Structures* 2012;49(3-4):420–435.
- [36] Rossi M, Lava P, Pierron F, Debruyne D, Sasso M. Effect of DIC spatial resolution, noise and interpolation error on identification results with the VFM. *Strain* 2015;51(3):206–222.
- [37] Maviglia F, Roccella S, Crescenzi F, Visca E, Carlini M. Impact of the monoblock thickness in an ITER-like configuration of DEMO divertor. *Fusion Engineering and Design* 2018;136:1322–1326.
- [38] Fursdon M, You JH, Li M. Towards reliable design-by-analysis for divertor plasma facing components—Guidelines for inelastic assessment (part 1: Unirradiated). *Fusion Engineering and Design* 2019;147:111234.
- [39] Fursdon M, You J. Towards reliable design-by-analysis for divertor plasma facing components—Guidelines for inelastic assessment (part II: Irradiated). *Fusion Engineering and Design* 2020;160:111831.
- [40] 2 ISIAAGMW, Testing advanced divertor concepts for fusion power plants using a small high heat flux facility; 2012.
- [41] Huber ML, Perkins RA, Assael M, Monogenidou S, Hellmann R, Sengers J. New international formulation for the thermal conductivity of heavy water. *Journal of Physical and Chemical Reference Data* 2022;51(1).
- [42] Sieder EN, Tate GE. Heat transfer and pressure drop of liquids in tubes. *Industrial & Engineering Chemistry* 1936;28(12):1429–1435.